

The new HyPix-3000 hybrid pixel array detector	2
Lab in the Spotlight Jerome B. Cohen X-Ray Diffraction Facility at Northwestern University	2
Southampton University takes a hands-on approach to teaching diffraction to undergraduates	3
Conferences and Workshops	4
Scientific Book Review	5
Material Analysis in the News	6
The Adventures of Captain Nano	7
Scientific Papers of Interest	8
Thin Film Training Textbook X-ray Diffraction Analysis for Thin Film Samples (Part 4)	10
Featured Rigaku Journal Article Size-strain analysis using the fundamental parameter (FP) method	19

Welcome

It is difficult for a native English speaker to learn Japanese (as I can personally attest to) and part of the difficulty is the use of different alphabets. In order to properly learn Japanese you must first learn to read it in the non-Romanized form, and that means learning three new alphabets: Hiragana, Katakana, and Kanji. Hiragana is a Japanese derived writing system, as is Katakana, but Katakana is reserved for writing words derived from foreign words. Kanji is the Chinese alphabet. To make it even more complicated, a single sentence can contain characters from all three writing systems.

As the May issue of The Bridge was being assembled, it struck me, that while most Rigaku products and customers utilize X-rays as a common technology, the “languages” they speak are quite different and there is a barrier involved in moving from one industry or science field to another. However, just as learning a new language can be a rewarding exercise, learning about a new industry or field of research can also broaden your horizons. So please view The Bridge as an opportunity to expand your knowledge of the overall field of X-ray technology by delving a little deeper and learning a new “language”.

Enjoy the newsletter.



BRIDGE 橋

A bridge is often used to symbolize a connection or link between two places, and thus we felt The Bridge would be the perfect name for our eNewsletter, as we hope that it will act as a vehicle for the transmission of ideas and information between Rigaku and interested readers around the world.

And a bridge is a two-way structure, a concept that we will keep in mind as we not only provide information about Rigaku, but also report on interesting research and the associated laboratories around the world, publish technical book reviews that might help our readers in their work, and highlight general news topics that are of interest to many people involved in materials analysis.





The new HyPix-3000 hybrid pixel array detector brings a whole new level of efficiency to your diffraction research

0D, 1D, and 2D capabilities in a single detector

One of the best features of the HyPix-3000 is the ability to use it for 0D, 1D and 2D applications. By building in such capabilities into a single detector, downtime between switching configurations is minimized.

[Click here for more information on Rigaku's HyPix-3000](#)

Lab in the Spotlight

Jerome B. Cohen X-Ray Diffraction Facility at Northwestern University

Facility Director: Prof. Michael Bedzyk, Materials Science & Engineering Department

Rigaku's latest instruments for powder XRD, thin-film XRD and small angle X-ray scattering have been installed in the Jerome B. Cohen X-Ray Diffraction Facility at Northwestern University, Evanston, Illinois, USA. A 1970s vintage Rigaku powder diffractometer and Rigaku's powerful high-intensity rotating anode generators are also installed in this same room. The equipment is well maintained by Jerry Carsello, facility manager, and all of the equipment is functioning well.



Prof. Bedzyk (left) and Jerry Carsello, Facility Manager

Students and researchers can use these instruments for their fundamental experiments in physics, as well as for complicated research.

Use of the instruments is not limited to the university's students, faculty and researchers. Applicants from outside of the university are also able to use them. "More than 300 users are accessing this facility for the research of material science and physics," said Prof. Bedzyk, facility director.

Several standalone rotating anode X-ray generators are combined with special optics and goniometers to simulate the experiments at the synchrotron. Northwestern is located near the Advanced Photon Source (APS), a third-generation synchrotron, so the Northwestern facility is used for hardware development and pre-measurement before going to the APS.

The research group run by Prof. Bedzyk is focusing on atomic scale views of interfacial and nanoscale processes with X-rays, using a combination of the instruments in this shared facility and APS.

The following recent research article, by Dr. Sumit Kewalramani in the Betzyk group, describes one example of how the group is using the X-ray diffraction facility. He measured GIXRD and XRR with a Rigaku ATX-G Thin-film XRD to generate the results presented in this paper.

"In-Situ Probe of Gate Dielectric-Semiconductor Interfacial Order in Organic Transistors: Origin and Control of Large Performance Sensitivities", Stephanie R. Walter, Jangdae Youn, Jonathan D. Emery, Sumit Kewalramani, Jonathan W. Hennek, Michael J. Bedzyk, Antonio Facchetti, Tobin J. Marks, Franz M. Geiger, *J. Am. Chem. Soc.* **134**, 11726-11733 (2012)

In this article, the classic "buried interface" problem of organic thin-film transistor performance was explored. The results of this experiment are impressive

There is also "iLab", which is one of the most interesting elements of the educational program at Northwestern University. This remote online lab program for high school science is exceptionally popular among high school students and teachers. High school students can access the internet-based program anytime they want to study. They can also gain experience in analytical instrument operation. There is a fully functional educational program related to ICP, and more is planned.



Prof. Kemi Jona (right) and Ashley Walter, Coordinator of XRD iLab

According to Prof. Kemi Jona, the director of the high-school science program, more than 8,000 students and teachers around the world have used "iLab". Users come from a broad range of geographies and backgrounds, including students from the US, Australia, Europe, South Africa and Asia. MIT and Sydney University have

joined in the effort and, in collaboration with Northwestern, are also offering educational materials for "iLab" targeting high school students.

Included in the mix will be a new material science class centered on powder diffraction analysis. The new course will be launched this summer, with a focus on forensic investigation using a Rigaku DMAX/B PXRD. Ashley Walter, project coordinator is preparing the summer "iLab" program for XRD.

Rigaku looks forward to working with the university to ensure that practical experience with XRD instruments is offered to high school students interested in material science around the world.

At present, the following Rigaku X-ray instruments are installed at Northwestern University:

- SmartLab Thin-film Diffractometer
- Ultima IV for Powder XRD
- ATX-G Thin-film Diffractometer
- S-MAX3000 High Brilliance SAXS System
- DMAX/A Powder XRD (x2)
- DMAX/B Powder XRD
- Three rotating anode generators



Utilizing Benchtop Instruments in a Teaching Environment

Southampton University takes a hands-on approach to teaching diffraction to undergraduates

Southampton University takes diffraction seriously. In this video you will see the high-powered lab that acts as the National Crystallographic Service in the UK, and hear about the use of benchtop instruments for teaching hands-on diffraction to third year undergraduates.

[Click here to watch video](#)

Conferences and Workshops

Rigaku is entering the busy time of tradeshows, exhibitions, and training classes. Pictures shown in this section are students who participated in a recent training event in Rigaku's Houston, Texas facility.

Rigaku will be sponsoring, attending or exhibiting at the following conferences and trade shows:

47th (Erice) Structure and Function from Macromolecular Crystallography

Erice, Italy

May 30 – June 8

95th Canadian Chemistry Conference

Vancouver, Canada

June 1 – 5

CPhi Istanbul

Istanbul, Turkey

June 4 – 6

[Click here to see the complete list](#)



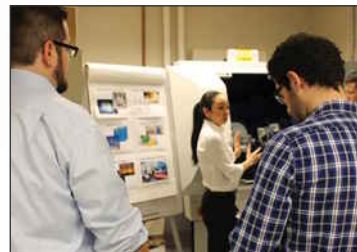
Featured Rigaku Journal Article

Size-strain analysis using the fundamental parameter (FP) method

Dr. Akihiro Himeda, Application & Software Development, Rigaku Corporation

Nano-sized material continues to receive a large amount of attention in the material science field, and correspondingly, crystallite size and strain evaluation from X-ray powder diffraction is becoming increasingly important. Rigaku's PDXL, integrated application software for XRPD, supports a fundamental parameters (FP) approach to calculate instrumental broadening on diffraction patterns and it enables one to evaluate crystallite size and strain more accurately and easily. In this paper, a test result of a round robin organized by the IUCr and an application example on ZnO nano-particles assuming different shape models are discussed.

[Click here for full article](#)



Scientific Book Review

Celestial Sleuth: Using Astronomy to Solve Mysteries in Art, History, and Literature
By Donald W. Olson

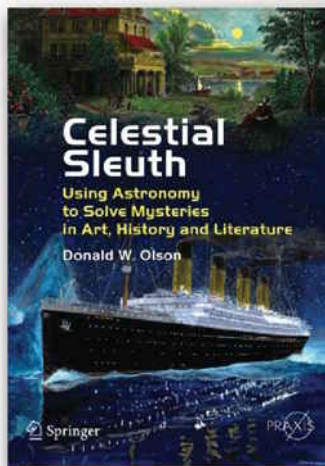
Springer Praxis Books, New York, 2014, 355 pages.
ISBN 978-1-4614-8403-5

It may not seem like the unsolved mysteries of art, history, and literature could have anything to do with astronomy, but physicist Donald W. Olson seeks to prove otherwise in his new book, *Celestial Sleuth*. As the title suggests, Olson implements the tools of astronomy to solve a select number of mysteries in these fields. The book should be just as enjoyable for a lover of art as a fan of physics. Despite the somewhat complicated astronomical theories applied to solve these “mysteries,” Olson does a decent job of explaining these concepts so that the average layman can understand exactly how he solves them.

First, Olson seeks to answer a number of questions about the time and location, as well as the celestial accuracy of a number of famous paintings, including those by Monet, van Gogh, and Munch. Olson and his team used celestial markers in the paintings to determine the exact time and location of the scenes depicted in the paintings.

Then, Olson approaches a series of historical questions. I found his interest in debunking the urban legend that the Boston Tea Party occurred under a full moon quite intriguing. As Olson and his team eventually proved, the Boston Tea Party really occurred under the cover of almost total darkness, as the moon would have been a thin waxing crescent on that night.

Finally, Olson wraps up the book with an astronomically driven approach to literature, which he breaks into two categories, pre-1800 and post-1800. Of these discussions, I was most intrigued by Olson’s interest in Shakespeare’s *Hamlet* and its description of a “bright star” burning in the first act. He ultimately reaches the conclusion that Shakespeare was actually describing a famous supernova that happened in 1572. As a budding Shakespearean scholar, I found it interesting that such a brief yet iconic moment in one of his works could in fact be rooted in a real-life astronomical event.



I found it particularly helpful that the book has numerous illustrations, including reproductions of the paintings Olson discusses, relevant photographs of the night sky and landscape, as well as a few documentary photographs of Olson and his team from Texas State University.

I wasn’t sure what to expect when I began reading this book, and although at times it seemed to me like Olson used astronomy as an umbrella concept under which to draw conclusions about art, history and literature, it was a good and relatively quick read.

Jeanette S. Ferrara,
Princeton, Class of 2015



Thin Film Training Textbook

Overview of the principles of X-ray reflectivity (Part 5)

If the surface and the interfaces are flat, the X-ray reflectivity method can be used whether the sample is crystalline or amorphous. X-ray reflectivity has drawn particular attention as a measurement technique capable of evaluating the film thickness, density, and surface or interface roughness of the thin-film materials used in semiconductor devices.

This month we start a chapter that provides an overview of the principles of X-ray reflectivity, measurement procedures, and analysis methods. It also discusses the procedural flow from measurement to analysis, as well as precautions.

[Click here for Part 5](#)

Material Analysis in the News

May 2, 2014. Stanford Linear Accelerator Center (SLAC) researchers have made the first direct measurements of a small and extremely rapid atomic rearrangement, associated with a class called [martensitic transformations](#), that dramatically changes the properties of many important materials, such as doubling the hardness of steel and causing shape-memory alloys to revert to a previous shape.

May 9, 2014. Scientists at the University of Illinois at Urbana-Champaign, USA; Argonne National Lab, USA; Centre for Free-Electron Laser Science, Hamburg, Germany and University College London, UK have developed a new technique called [rotational X-ray tracking \(RXT\)](#). The researchers were successful in demonstrating the power of the new technique by using it to study small crystalline particles immobilized by the fact they form a colloidal gel under certain conditions.

May 12, 2014. Google honors [Dorothy Hodgkin's X-ray vision](#) with a molecular doodle. The event marks the 104th anniversary of the British chemist, who pioneered the use of X-rays to determine the structure of biological molecules.

May 13, 2014. Combining different approaches including optical microscopy, electron microscopy, Raman spectroscopy and synchrotron X-ray techniques, an international team of researchers showed that the crystals contained in the 'Oil spot' Jian bowl glaze – of ancient Chinese pottery – were responsible for the silvery patterns. They consist of a [high purity \$\epsilon\$ -Fe₂O₃ phase](#) (the epsilon phase), a very rare and metastable relative of the mineral hematite.

May 14, 2014. Sheepskin has long been considered a low value product because of its lack of strength and stability, and its structure is made weaker when the wool is removed. New research, using small angle X-ray scattering (SAXS), has helped identify the fundamental aspects of the collagen network that contribute to the [intrinsic strength of leather](#).

May 15, 2014. World-renowned scholar [Dr. Peter Michael Rentzepis](#) recently joined the faculty of the Department of Electrical and Computer Engineering at Texas A&M University as professor and holder of the TEES Distinguished Research Professorship.

May 18, 2014. [Sodium manganese dioxide](#) has shown promise for use in electrodes in rechargeable batteries. Now a team of researchers has produced the first detailed visualization – down to the level of individual atoms – of exactly how the material behaves during charging and discharging, in the process elucidating an exotic molecular state that may help in understanding superconductivity.

May 20, 2014. [SAFC and BioTools partner to speed chiral clients to market](#). SAFC and BioTools have formed a partnership to provide a unified services to companies making chiral-based drugs. SAFC will bring to the partnership its X-ray diffraction technology.

May 20, 2014. A [new report studies the global atomic spectroscopy market](#) over the forecast period of 2013 to 2018. The market was valued at \$4.02 billion in 2013 and is expected to reach \$5.5 billion by 2018, growing at a CAGR of 6.4% from 2013 to 2018.

May 21, 2014. [Dr. Scott T. Misture](#), Inamori Professor of Materials Science and Engineering in the Kazuo Inamori School of Engineering at Alfred University (AU), has been named a Fellow of The American Ceramic Society (ACerS).

The Adventures of Captain Nano

GUS THE GUINEA PIG — Dr. F. Furter expands his ability to control nano structures.

Captain Nano - Gus the Guinea Pig

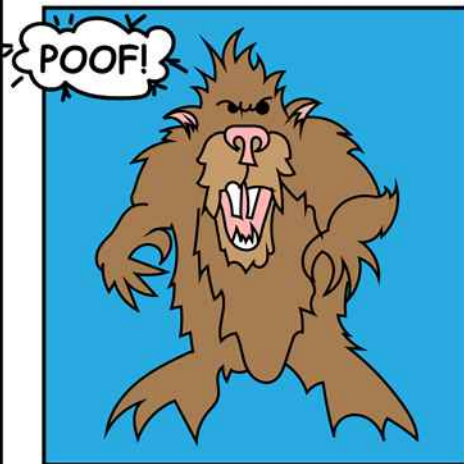
WHILE DR. F. CONTINUES TO IMPROVE HIS IMAGE AT NANO-LEVEL, HE DECIDES TO EXPAND ON HIS EXPERIMENT. AT NORMAL SIZE, OUR HERO RETURNS TO THE LAB TO DISCOVER THIS ACTIVITY.



Oh no! It seems Dr. Frank Furter has determined how to manipulate structures at nano levels



Yes, my friend. You will do my bidding and kill those RATS.



© 20140526 Adam Courville

Recent Scientific Papers of Interest

Characterization of a Fluidized Catalytic Cracking Catalyst on Ensemble and Individual Particle Level by X-ray Micro- and Nanotomography, Micro-X-ray Fluorescence, and Micro-X-ray Diffraction. Bare, Simon R.; Charochak, Meghan E.; Kelly, Shelly D.; Lai, Barry; Wang, Jun; Chen-Wiegart, Yu-chen Karen. *ChemCatChem*. May2014, Vol. 6 Issue 5, p1427-1437. 11p.
[DOI: 10.1002/cctc.201300974](https://doi.org/10.1002/cctc.201300974).

Order of Magnitude Sensitivity Increase in X-ray Fluorescence Computed Tomography (XFCT) Imaging With an Optimized Spectro-Spatial Detector Configuration: Theory and Simulation. Ahmad, Moiz; Bazalova, Magdalena; Xiang, Liangzhong; Xing, Lei. *IEEE Transactions on Medical Imaging*. May2014, Vol. 33 Issue 5, p1119-1128. 10p.
[DOI: 10.1109/TMI.2014.2305101](https://doi.org/10.1109/TMI.2014.2305101).

Effect of bainitic transformation temperature on the mechanical behavior of cold-rolled TRIP steels studied with *in-situ* high-energy X-ray diffraction. Fu, B.; Yang, W.Y.; Li, L.F.; Sun, Z.Q. *Materials Science & Engineering: A*. May2014, Vol. 603, p134-140. 7p.
[DOI: 10.1016/j.msea.2014.02.082](https://doi.org/10.1016/j.msea.2014.02.082).

X-Ray diffraction study of the microstructure of C60 fullerite powder after grinding in a planetary ball mill. Sirotinkin, V.; Agafonov, S. *Inorganic Materials*. May2014, Vol. 50 Issue 5, p464-468. 5p. [DOI: 10.1134/S0020168514050161](https://doi.org/10.1134/S0020168514050161).

Characterization of morphology and hydration products of high-volume fly ash paste by monochromatic scanning x-ray micro-diffraction (μ -SXRD). Bae, Sungchul; Meral, Cagla; Oh, Jae-eun; Moon, Juhuk; Kunz, Martin; Monteiro, Paulo J.M. *Cement & Concrete Research*. May2014, Vol. 59, p155-164. 10p.
[DOI: 10.1016/j.cemconres.2014.03.001](https://doi.org/10.1016/j.cemconres.2014.03.001).

Multi-scale X-ray diffraction study of strains induced by He implantation in UO_2 polycrystals. Richard, A.; Castelier, E.; Palancher, H.; Micha, J.S.; Rouquette, H.; Ambard, A.; Garcia, Ph.; Goudeau, Ph. *Nuclear Instruments & Methods in Physics Research Section B*. May2014, Vol. 326, p251-255. 5p.
[DOI: 10.1016/j.nimb.2013.10.057](https://doi.org/10.1016/j.nimb.2013.10.057).

A new theory for X-ray diffraction. Fewster, Paul F. *Acta Crystallographica. Section A, Foundations & Advances*. May2014, Vol. 70 Issue 3, p257-282. 26p.
[DOI: 10.1107/S205327331400117X](https://doi.org/10.1107/S205327331400117X).

Characterization of unprocessed historic platinum photographic papers by Raman, FTIR and XRF. Centeno, Silvia A.; Vila, Anna; Barro, Lisa. *Microchemical Journal*. May2014, Vol. 114, p8-15. 8p.
[DOI: 10.1016/j.microc.2013.11.016](https://doi.org/10.1016/j.microc.2013.11.016).

***In situ* X-ray diffraction monitoring of GaInN/GaN superlattice during organometallic vapor phase epitaxy growth.** Yamamoto, Taiji; Iida, Daisuke; Kondo, Yasunari; Sowa, Mihoko; Umeda, Shinya; Iwaya, Motoaki; Takeuchi, Tetsuya; Kamiyama, Satoshi; Akasaki, Isamu. *Journal of Crystal Growth*. May2014, Vol. 393, p108-113. 6p.
[DOI: 10.1016/j.jcrysgro.2013.11.072](https://doi.org/10.1016/j.jcrysgro.2013.11.072).

Preparation of metal oxide nanoparticles of different sizes and morphologies, their characterization using small angle X-ray scattering and study of thermal properties. Gopinath, S.; Philip, John. *Materials Chemistry & Physics*. May2014, Vol. 145 Issue 1/2, p213-221. 9p.
[DOI: 10.1016/j.matchemphys.2014.02.005](https://doi.org/10.1016/j.matchemphys.2014.02.005).

Stretching induced phase separation in poly(vinylidene fluoride)/poly(butylene succinate) blends studied by *in-situ* X-ray scattering. Liu, Guoming; Schneider, Konrad; Zheng, Liuchun; Zhang, Xiuqin; Li, Chuncheng; Stamm, Manfred; Wang, Dujin. *Polymer*. May2014, Vol. 55 Issue 10, p2588-2596. 9p.
[DOI: 10.1016/j.polymer.2014.03.055](https://doi.org/10.1016/j.polymer.2014.03.055).

Small-angle X-ray scattering studies on melting and recrystallization behaviors of poly(oxyethylene) crystallites in poly(d,l-lactide)/poly(oxyethylene) blends. Tien, Nguyen-Dung; Sasaki, Sono; Masunaga, Hiroyasu; Shimizu, Nobutaka; Igarashi, Noriyuki; Sakurai, Shinichi. *Polymer*. May2014, Vol. 55 Issue 10, p2562-2569. 8p.
[DOI: 10.1016/j.polymer.2014.03.048](https://doi.org/10.1016/j.polymer.2014.03.048).

Thermal expansion measurements by x-ray scattering and breakdown of Ehrenfest's relation in alloy liquids. Gangopadhyay, A. K.; Blodgett, M. E.; Johnson, M. L.; Vogt, A. J.; Mauro, N. A.; Kelton, K. F. *Applied Physics Letters*. 5/12/2014, Vol. 104 Issue 19, p1-5. 5p. 1 Chart, 4 Graphs. [DOI: 10.1063/1.4876125](https://doi.org/10.1063/1.4876125).

Evolution and change of He bubbles in He-containing Ti films upon thermal treatment studied by small-angle X-ray scattering and transmission electron microscopy. Sun, Guangai; Wu, Erdong; Huang, Chaoqiang; Cheng, Chun; Yan, Guanyun; Wang, Xiaolin; Liu, Shi; Tian, Qiang; Chen, Bo; Wu, Zhonghua; Liu, Yi; Wang, Jie. *Thin Solid Films*. May2014, Vol. 558, p125-133. 9p.
[DOI: 10.1016/j.tsf.2014.03.005](https://doi.org/10.1016/j.tsf.2014.03.005).

X-ray Scattering Evaluation of Ultrastructural Changes in Human Dental Tissues with Thermal Treatment. Sandholzer, Michael A.; Sui, Tan; Korsunsky, Alexander M.; Damien Walmsley, Anthony; Lumley, Philip J.; Landini, Gabriel. *Journal of Forensic Sciences (Wiley-Blackwell)*. May2014, Vol. 59 Issue 3, p769-774. 6p.
[DOI: 10.1111/1556-4029.12400](https://doi.org/10.1111/1556-4029.12400).

Phase-based x-ray scattering--A possible method to detect cancer cells in a very early stage. Feye-Treimer, U.; Treimer, W. *Medical Physics*. May2014, Vol. 41 Issue 5, p1-12. 12p.
[DOI: 10.1118/1.4871616](https://doi.org/10.1118/1.4871616).

Small angle X-ray scattering investigation of multiarm star sulfonated polystyrene based ionomer membranes. Batat, Pinar; Bilir, Çiğdem; Erdogan, Tuba; Levent Demirel, A. *European Polymer Journal*. May2014, Vol. 54, p79-86. 8p.
[DOI: 10.1016/j.eurpolymj.2014.02.013](https://doi.org/10.1016/j.eurpolymj.2014.02.013).

Search for photon–photon elastic scattering in the X-ray region. Inada, T.; Yamaji, T.; Adachi, S.; Namba, T.; Asai, S.; Kobayashi, T.; Tamasaku, K.; Tanaka, Y.; Inubushi, Y.; Sawada, K.; Yabashi, M.; Ishikawa, T. *Physics Letters B*. May2014, Vol. 732, p356-359. 4p.

[DOI: 10.1016/j.physletb.2014.03.054.](https://doi.org/10.1016/j.physletb.2014.03.054)

Examination of CoNiCu thin films by using XRF and XRD. Söğüt, Ö.; Dönük, Ç.; Apaydin, G.; Bakkaloğlu, Ö.F. *Canadian Journal of Physics*. May2014, Vol. 92 Issue 5, p435-439. 5p. 3 Black and White Photographs, 1 Chart, 5 Graphs.

[DOI: 10.1139/cjp-2012-0538.](https://doi.org/10.1139/cjp-2012-0538)

Analysis of a royal 15th century illuminated parchment using a portable XRF–XRD system and micro-invasive techniques. Duran, A.; López-Montes, A.; Castaing, J.; Espejo, T. *Journal of Archaeological Science*. May2014, Vol. 45, p52-58. 7p. [DOI: 10.1016/j.jas.2014.02.011.](https://doi.org/10.1016/j.jas.2014.02.011)

HRTEM, SAED and XRD investigations of RE₄O₄[AsO₄]Cl (RE =La, Pr, Nd, Sm, Eu, Gd). Ben Yahia, Hamdi; Rodewald, Ute Ch.; Boulahya, Khalid; Pöttgen, Rainer. *Materials Research Bulletin*. May2014, Vol. 53, p257-265. 9p.

[DOI: 10.1016/j.materresbull.2014.02.025.](https://doi.org/10.1016/j.materresbull.2014.02.025)

Swelling induced by alpha decay in monazite and zirconolite ceramics: A XRD and TEM comparative study. Deschanel, X.; Seydoux-Guillaume, A.M.; Magnin, V.; Mesbah, A.; Tribet, M.; Moloney, M.P.; Serruys, Y.; Peugeot, S. *Journal of Nuclear Materials*. May2014, Vol. 448 Issue 1-3, p184-194. 11p.

[DOI: 10.1016/j.jnucmat.2014.02.003.](https://doi.org/10.1016/j.jnucmat.2014.02.003)

Comparison of XRD, XANES and TGA methods to assess the O/M ratio of Th_{0.60}Am_{0.40}O_{2-x}. Prieur, D.; Vigier, J.-F.; Rothe, J.; Somers, J. *Journal of Nuclear Materials*. May2014, Vol. 448 Issue 1-3, p4-7. 4p. [DOI: 10.1016/j.jnucmat.2014.01.031.](https://doi.org/10.1016/j.jnucmat.2014.01.031)



X-ray Diffraction Analysis for Thin Film Samples

Training Textbook

Click below to see previously published sections

<i>X-ray Diffraction Analysis for Thin Film Samples (Part 1)</i>	<i>January 2014, Issue 7</i>
<i>X-ray Diffraction Analysis for Thin Film Samples (Part 2)</i>	<i>February 2014, Issue 8</i>
<i>X-ray Diffraction Analysis for Thin Film Samples (Part 3)</i>	<i>March 2014, Issue 9</i>
<i>X-ray Diffraction Analysis for Thin Film Samples (Part 4)</i>	<i>April 2014, Issue 10</i>

Chapter 4

Reflectivity Method

If the surface and the interfaces are flat, the X-ray reflectivity method can be used whether the sample is crystalline or amorphous. X-ray reflectivity has drawn particular attention as a measurement technique capable of evaluating the film thickness, density, and surface or interface roughness of the thin-film materials used in semiconductor devices.

This chapter provides an overview of the principles of X-ray reflectivity, measurement procedures, and analysis methods. It also discusses the procedural flow from measurement to analysis, as well as precautions.

4.1 Applicability of X-Ray Reflectivity Method

Thin-film materials have found use in a wide range of devices in recent years, gaining the status of an essential category of advanced materials. The diverse characteristics of the devices depend significantly on the thickness, density, and surface or interface roughness of thin-film materials. These parameters must be correctly evaluated and film growth conditions properly controlled.

Used to evaluate these parameters, X-ray reflectivity involves X-ray incidence at grazing angles with respect to sample surfaces. The method is used to analyze X-ray reflection intensity profiles versus incident angles and to determine structural parameters (thickness, density, and surface or interface roughness) of the thin film in question. Areas of application are given below. X-ray reflectivity can be used to do the following:

1. Measure thickness from several to several thousand nanometers.
2. Evaluate the surface roughness and interface width (arising from roughness and interdiffusion).
3. Evaluate the density of the film of known composition.
4. Evaluate the structure of a multilayer or single layer film.
5. Perform these tasks with a wide range of materials, whether crystalline or amorphous, including semiconductors and superconducting, magnetic, metal, and polymer films.
6. Measure samples nondestructively.

4.2 Overview of X-Ray Reflectivity Method

When X-rays are incident at a grazing angle to a flat surface of a material, **total reflection** occurs below incident angle θ_c . This angle is called the **total reflection critical angle** (critical angle hereafter). The critical angle for the Cu $K\alpha$ line is small, with values such as 0.22° for Si, 0.42° for Ni, and 0.57° for Au and changes with the electron density (refractive index) of the material. As the X-ray incident angle increases to values beyond this angle, the X-rays gradually penetrate deeper into the material. In a material with ideal planes, reflectivity rapidly decreases proportionally to θ^{-4} at angles equal to or larger than θ_c , decreasing faster with substances having rough surfaces.

If a substrate composed of such a material is overlaid with a material having a differing electron density, the X-rays reflected on the interface between the substrate and the film and the X-rays reflected from the surface of the film will interfere constructively or destructively. This interference is visible as an oscillation in the reflectivity profile. First observed by Kiessig in 1931, this oscillation is known as the **Kiessig fringe**.

Fig. 4.2.1 shows the reflectivity profile of a Au film deposited on a Si substrate by sputtering. The graph shows the results of measurement for three types of films with thicknesses differing by approximately 10 nm.

4.2 Overview of X-Ray Reflectivity Method

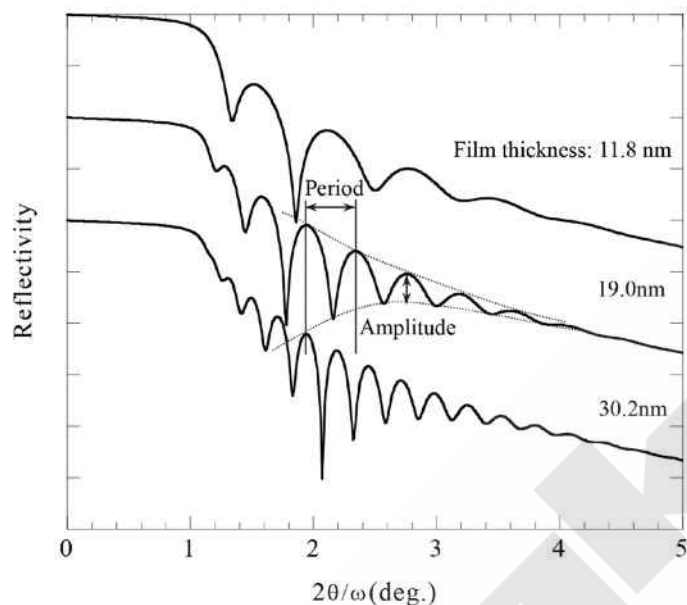


Figure 4.2.1. Reflectivity of Au film/Si substrate

The results indicate that the period of the oscillation provides information on the film thickness. The amplitude of the oscillation is angle-dependent and contains information on film density and surface or interface roughness. The X-ray reflectivity method analyzes this profile to obtain film thickness, density, and surface or interface roughness.

Listed below are examples of methods other than the X-ray reflectivity method for measuring film thickness.

1. Optical methods (such as an ellipsometer)
2. Cross-sectional TEM or SEM method
3. X-ray fluorescence method

The X-ray reflectivity method differs from these methods in the following ways:

Optical methods have the disadvantage that they cannot be applied to opaque films. X-ray reflectivity can be used with opaque films, including those made of metal.

The cross-sectional TEM method is a destructive method that involves complex sample preparations. X-ray reflectivity is nondestructive and allows measurements to be performed in air.

The X-ray fluorescence method obtains the mass of the analyzed element per unit volume through quantitative analysis and cannot provide film thickness directly. It also requires a reference sample, and precision declines with film thickness. The method makes it difficult to analyze samples with interdiffusion and cannot be used with systems containing layers of similar materials. The reflectivity method, in contrast, can be used in these cases—a major advantage.

The X-ray reflectivity method has the following characteristics:

1. The sample must be sufficiently flat and smooth. (Surface or interface roughness must be on the order of several nanometers or less.)
2. It can be applied to polycrystalline and amorphous materials.
3. It is extremely sensitive to surface states.
4. It is independent of crystal orientation or strain.
5. It is insensitive to changes in composition.
6. It can be used to evaluate film thicknesses of up to approximately 1,000 nm. It is not ideal for thicker films.

4.3 Principles of X-ray Reflectivity Method

4.3.1 Total Reflection and Refractive Index for X-Rays

Since the **refractive index** of a material for X-rays is slightly less than 1, the X-rays undergo total reflection when incident on a flat surface of a material at a grazing angle.

The refractive index n of a material for X-rays is given by Formula 4.3.1.

$$n = 1 - \delta - i\beta \quad \text{Formula 4.3.1}$$

$$\delta = \left(\frac{r_e \lambda^2}{2\pi} \right) N_0 \rho \sum_i x_i (z_i + f'_i) / \sum_i x_i M_i \quad \text{Formula 4.3.2}$$

$$\beta = \left(\frac{r_e \lambda^2}{2\pi} \right) N_0 \rho \sum_i x_i f''_i / \sum_i x_i M_i \quad \text{Formula 4.3.3}$$

r_e : Classical radius of an electron (2.818×10^{-9} m)

N_0 : Avogadro number

λ : X-ray wavelength

ρ : Density (g/cm^3)

z_i : Atomic number of the i -th atom

M_i : Atomic weight of the i -th atom

x_i : Atomic ratio (molar ratio) of the i -th atom

f'_i, f''_i : Atomic scattering factors of the i -th atom (anomalous dispersion term)

As suggested by Formula 4.3.1, the refractive index is expressed as a complex number. The parameter δ in the formula is of the order of magnitude of 10^{-5} to 10^{-6} for X-rays at wavelengths of approximately 1 Å and depends on X-ray wavelength and the density and composition of the material. An additional 1 to 2 orders of magnitude smaller, the parameter β is a quantity related to X-ray absorption, expressed by linear absorption coefficient μ in the following formula.

4.3 Principles of X-ray Reflectivity Method

$$\beta = \lambda\mu / 4\pi$$

Formula 4.3.4

If we disregard absorption, the critical angle θ_c for total reflection is given by the following formula:

$$\theta_c = \sqrt{2\delta}$$

Formula 4.3.5

Thus, we can obtain the density of the surface film from the total reflection critical angle. When the incident angle is less than the critical angle, the incident X-ray beam undergoes total reflection. If absorption is ignored, the reflected X-ray beam has approximately the same intensity as the incident X-ray beam (reflectivity is 1.0). If the incident angle is greater than the critical angle, the X-ray beam is refracted, and reflectivity rapidly decreases roughly in proportion to the value of the incident angle to a power of -4. The critical angle is usually 0.2° to 0.5°. It is generally greater with longer X-ray wavelengths and when the material is composed of heavier elements of greater density—in short, when the material has greater average electron density.

4.3.2 Reflected Wave and Refracted Wave

When the total reflection phenomenon occurs, the incident wave generates a specularly reflected wave and a refracted wave, as shown in Fig. 4.3.1.



Figure 4.3.1. Reflection and refraction of X-rays at material surface

If the density of the material is uniform, the specular reflectivity of the X-ray beam of wavelength λ at an ideally flat surface depends on the incident angle θ and can be expressed by the following formulas:

Boundary conditions:

$$R(\theta) = \frac{(\theta - A)^2 + B^2}{(\theta + A)^2 + B^2}$$

Formula 4.3.6

$$A = \sqrt{\frac{(\theta^2 - 2\delta)^2 + 4\beta^2 + (\theta^2 - 2\delta)}{2}}$$

Formula 4.3.7

$$B = \frac{\beta}{A}$$

Formula 4.3.8

Fig. 4.3.2 shows the reflectivity of Si as given by Formula 4.3.6. It shows a rapid change at critical angle θ_c (near 0.2° here).

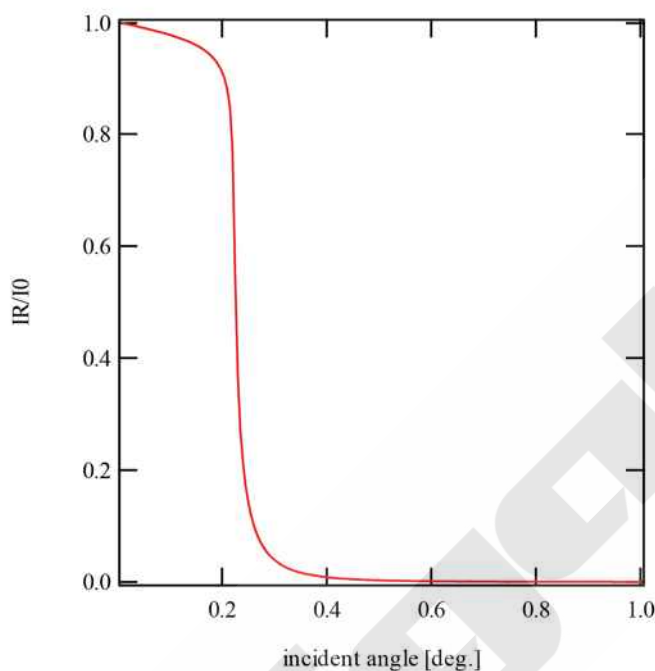


Figure 4.3.2. Reflectivity curve of Si

The intensity of the refracted wave decays exponentially in the depth direction (**evanescent wave**). For the incident angle θ , the intensity at depth z is expressed by the following formulas:

$$I(\theta, z) = S(\theta) \exp\left(-\frac{z}{D(\theta)}\right) \quad \text{Formula 4.3.9}$$

$$S(\theta) = \frac{4\theta^2}{(\theta + A)^2 + B^2} \quad \text{Formula 4.3.10}$$

$$D(\theta) = \frac{\lambda}{4\pi B^2} \quad \text{Formula 4.3.11}$$

Here, $S(\theta)$ is the X-ray intensity at the surface and $D(\theta)$ the penetration depth. Formula 4.3.9 applies to the case in which z is positive or zero. The intensity distribution for a negative value of z (the intensity distribution on the vacuum or gas side of the surface), is expressed by the following formula and indicates the interference caused by superposition with the reflected waves.

4.3 Principles of X-ray Reflectivity Method

$$I(\theta, z) = \frac{S(\theta)}{2\theta^2} [\theta^2 + A^2 + B^2 + (\theta^2 - A^2 - B^2)\cos\{\tau(\theta)\} + B\theta \sin\{\tau(\theta)\}] \tag{Formula 4.3.12}$$

$$\tau(\theta) = \frac{4\pi\theta}{\lambda}|z| \tag{Formula 4.3.13}$$

Similarly to Formula 4.3.9, $I(\theta, z) = S(\theta)$ when $z = 0$. Formula 4.3.12 indicates a standing wave forms with period $\lambda/2\theta$ at incident angle θ .

If the material has an interface at which the refractive index is discontinuous in the depth direction (as with a thin film on a substrate), we must consider the interference arising from multiple reflections at the interface. Rather than declining monotonically on reaching the critical angle, specular reflectivity oscillates, based on the interference. The intensity of the refracted wave has a complex distribution in the depth direction and cannot be expressed as an exponential function. To understand this behavior, consider the boundary conditions of the electric field vector at each interface in a generic multilayer model (Figure 4.3.3). As with uniform materials, we can calculate reflectivity by considering the boundary conditions of the electric field vector for the X-rays at each interface. Fig. 4.3.3

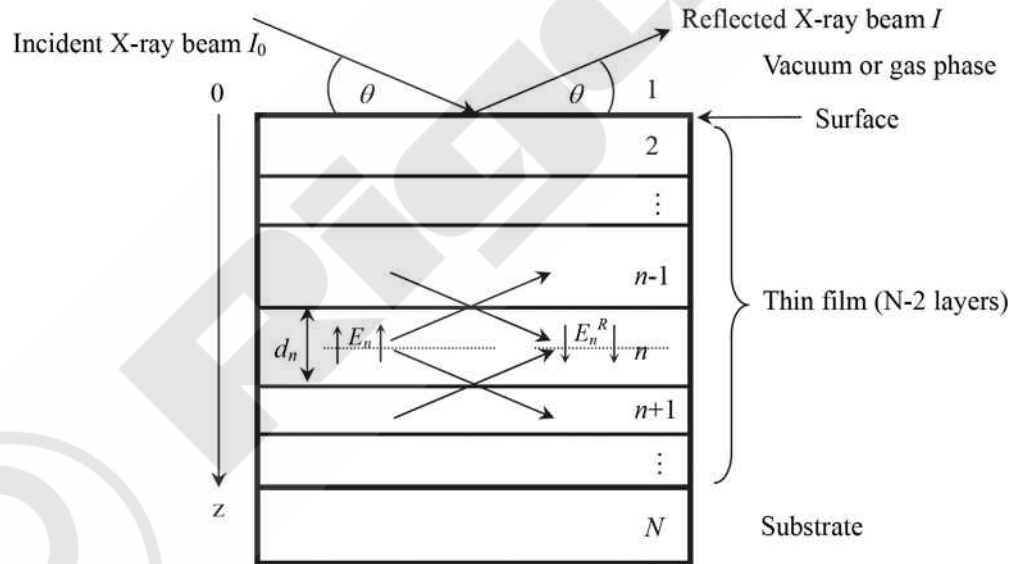


Figure 4.3.3. Multilayer film model

That is, when the amplitudes of the electric field vectors of the incident wave (wave propagating deeper) is denoted E_n and the reflected wave (wave propagating towards the surface) at the center of the n -th layer is denoted E_n^R , the continuity at the interface between the $(n-1)$ -th and n -th layers imposes the boundary conditions give by the formulas below:

$$a_{n-1}E_{n-1} + a_{n-1}^{-1}E_{n-1}^R = a_nE_n + a_nE_n^R \tag{Formula 4.3.14}$$

$$(a_{n-1}E_{n-1} + a_{n-1}^{-1}E_{n-1}^R)f_{n-1}k = (a_nE_n + a_nE_n^R)f_nk \tag{Formula 4.3.15}$$

Here, the parameters are expressed as follows:

$$k = \frac{2\pi}{\lambda} \quad \text{Formula 4.3.16}$$

$$f_n = \sqrt{\{(\theta^2 - 2\delta) - i2\beta\}} = A_n - iB_n \quad \text{Formula 4.3.17}$$

$$a_n = \exp\left(-i \frac{kf_n d_n}{2}\right) \quad \text{Formula 4.3.18}$$

The parameter d_n represents the thickness of the n -th layer. The parameter f_n is related to the Fresnel coefficient, $F_{n-1,n}$, by the following formula:

$$F_{n,n-1} = \frac{f_{n-1} - f_n}{f_{n-1} + f_n} \quad \text{Formula 4.3.19}$$

A_n and B_n are quantities given by Formula 4.3.6 for the material in the n -th layer. The parameter a_n gives the phase difference generated when the X-ray beam propagates half the thickness of the layer and the phase difference when waves reflected from the interfaces interfere with each other.

We can calculate reflection coefficient $R_{n-1,n}$ ($= \alpha_{n-1}^2 E_n^R / E_n^I$) at the interface between the $(n-1)$ -th and n -th layers by applying Formulas 4.3.14, 4.3.15, and 4.3.19, and express the relationships in a recurrence formula:

$$R_{n-1,n} = a_{n-1}^4 \frac{R_{n,n+1} + F_{n-1,n}}{R_{n,n+1} F_{n-1,n} + 1} \quad \text{Formula 4.3.20}$$

If we assume that the substrate is sufficiently thick and that we can disregard the possibility of reflections from the rear side—that is, that $R_{n,n+1} = 0$ —we can calculate the reflection coefficients of the interfaces one by one from the lowest interface towards the surface using Formula 4.3.20. Finally, the formula below gives specular reflectivity:

$$R(\theta) = \frac{I}{I_0} = |R_{1,2}|^2 \quad \text{Formula 4.3.21}$$

Reference: L. G. Parratt; Phys. Rev., **95**, 359 (1954)

4.3.3 Effects of Roughness

Most measurement samples do not have an ideally flat surface. Roughness at the surface or at interfaces affect reflectivity measurements. Assume that the position of the interface between the $(n-1)$ -th and n -th layers is expressed by a Gaussian distribution and that **root mean square (rms) roughness** is σ_{n-1} . Then, the Fresnel coefficient can be corrected as shown in the formula below using scattering vectors q_{n-1} and q_n at the interface.

$$F'_{n-1,n} = F_{n-1,n} \exp\left(-\frac{\sigma_{n-1}^2 q_{n-1} q_n}{2}\right) \quad \text{Formula 4.3.22}$$

4.3 Principles of X-ray Reflectivity Method

Here, for scattering with equal angles such as specular scattering, the scattering vectors are expressed as follows:

$$q_{n-1} = 2kf_{n-1} = \frac{4\pi}{\lambda} f_{n-1} \quad \text{Formula 4.3.23}$$

We can calculate specular reflectivity with Formula 4.3.20 by substituting the correction of Formula 4.3.22 for the Fresnel coefficient. The specular reflectivity of a uniform system without a layered structure is calculated using the following formula, instead of Formula 4.3.6:

$$R(\theta) = \frac{(\theta - A)^2 + B^2}{(\theta + A)^2 + B^2} \exp\left(-\frac{16\pi^2}{\lambda^2} \sigma^2 \theta A\right) \quad \text{Formula 4.3.24}$$

Reference: L. Nevot and P. Croce;, **15**, 761 (1980)

Size-strain analysis using the fundamental parameter (FP) method

Akihiro Himeda*

1. Background

Crystallite size and strain affect the physical (mechanical, electric, magnetic and optical) properties of materials. It is quite important to quantify size and strain, and to clarify the relationship between them in the field of material science.

The effects of finite crystallite size and lattice strain can be observed as deformations in the shape of diffraction curves. Thus, information can be obtained by investigating their shapes. However, the deformation occurs due to not only size-strain effects but also instrumental effects.

In conventional estimation, only the width of the peaks is used, not the whole peak shape. To eliminate the instrumental effect, width correction is carried out by measuring standard samples and subtracting the breadths of peaks of the width standard sample from those of a sample being investigated. With the 2-theta dependence of the corrected peak width, we can extract the crystallite size and lattice strain quantities.

However, the method of subtraction depends on whether the peak shape is assumed to be Gaussian or Lorentzian. In addition to this, the peak shape will not necessarily express a Gaussian or Lorentzian function. Moreover, so-called “super Lorentzian” peak shapes are reported for samples with broader distribution of crystallite size. Based on this, applied width corrections may have limited validity.

In contrast to the above, the fundamental parameter method (FP method)⁽¹⁾ has recently been used to analyze the effect of profile shape originated from instrumental conditions. In the FP method, the peak shape is calculated by convoluting the instrumental profile shapes assuming a theoretical model of instrument and profiles originated from crystallite size and lattice strain. In this way, we can obtain size-strain information and eliminate the instrumental effects without measuring standard samples.

Size distribution can also be quantified by analyzing the precise peak shape. Size distribution affects the sharpness close to the peak top and slow fading off of its tails.

In PDXL 2⁽²⁾, crystallite size, size distribution and strain can be analyzed with the FP method more easily than the ordinary Rietveld method. In this report, theoretical background to analyze them and some

applications of actual samples using PDXL are described.

2. Crystallite size, size distribution and strain

X-ray profile diffracted from a spherical crystallite with its diameter D is expressed as⁽³⁾,

$$f_s(k; D) = \frac{3D}{s^2} \left[1 - \frac{2}{s} \sin s + \frac{4}{s^2} \sin^2 \left(\frac{s}{2} \right) \right]$$

Here,

$$s = 2\pi kD$$

and

$$k = 2(\sin(\theta + \Delta\theta) - \sin\theta) / \lambda \cong 2\Delta\theta \cos\theta / \lambda$$

Since actual powder samples consist of a lot of crystallites with varied diameters, the observable profile shape is formulated with an averaged function by the distribution function P of their diameters as:

$$f_s(k; D_0, C) = \int_0^\infty dD f_s(k; D) P(D; D_0, C)$$

Lognormal distribution is widely used for the distribution function. It is known that the size distribution obtained by means of electron microscopy is often closely lognormal. The function form is expressed as:

$$P(D; D_0, C) = \frac{1}{D\sqrt{2\pi \ln(1+C^2)}} \exp \left[-\frac{\left\{ \ln \left((D/D_0) \sqrt{1+C^2} \right) \right\}^2}{2 \ln(1+C^2)} \right]$$

Here, D_0 is a volume weighted mean diameter and C is a normalized standard deviation which expresses the broadness of the distribution. In Fig. 1, profile shape dependences in terms of C are shown. The red line shows the profile when $C=0.1$, assuming very narrow distribution of diameters, which is almost identical to that of a single spherical crystallite. As the distribution becomes broader ($C=1$ in green line and $C=1.5$ in blue line), the shape near the peak top becomes sharper and its tail trails more slowly. Since these three profiles have the same volume weighted mean diameter value, their peak widths do not correspond to the average diameter. This means the conventional size analysis used the peak breadth is quantitatively insufficient.

* Application & Software Development Department, X-ray Analysis Division, Rigaku Corporation.

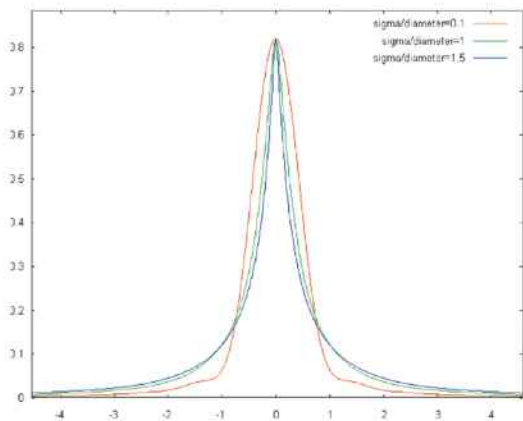


Fig. 1. Distribution width C dependences of the profile shape.

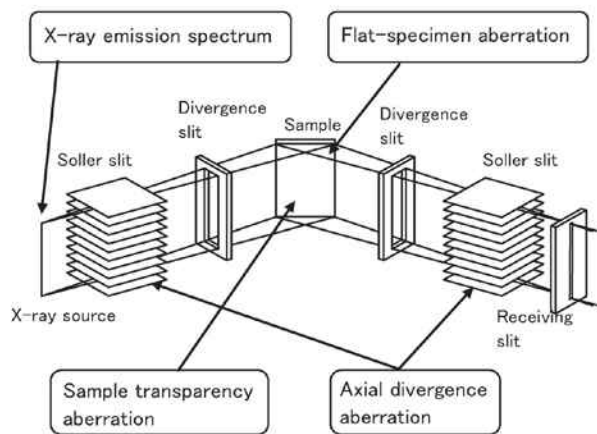


Fig. 2. Schematic diagram of a Bragg-Brentano diffractometer.

3. FP method

In the FP method, an observed profile is obtained by convoluting the profile from crystallites described in the previous section and those from instrumental aberration functions. In the case of Bragg-Brentano diffractometers, which are widely used for powder diffractometry, the instrumental functions are listed as follows:

- a. X-ray emission spectrum
- b. axial divergence aberration
- c. receiving-slit width function
- d. flat-specimen aberration
- e. sample-transparency aberration
- f. effective focus size

Typical profile shapes from the above aberration functions are shown in Fig. 3. Profile changes with convoluting aberration functions are shown in Fig. 4. Crystallite profile is given in red. Profiles from successively applied convolutions of emission spectrum, axial divergence, receiving-slit width, flat-specimen, sample-transparency, and effective focus size are shown in green, blue, pink, dark blue and brown, respectively. It is shown that the dominant effects in this case are from emission spectrum and axial divergence aberration.

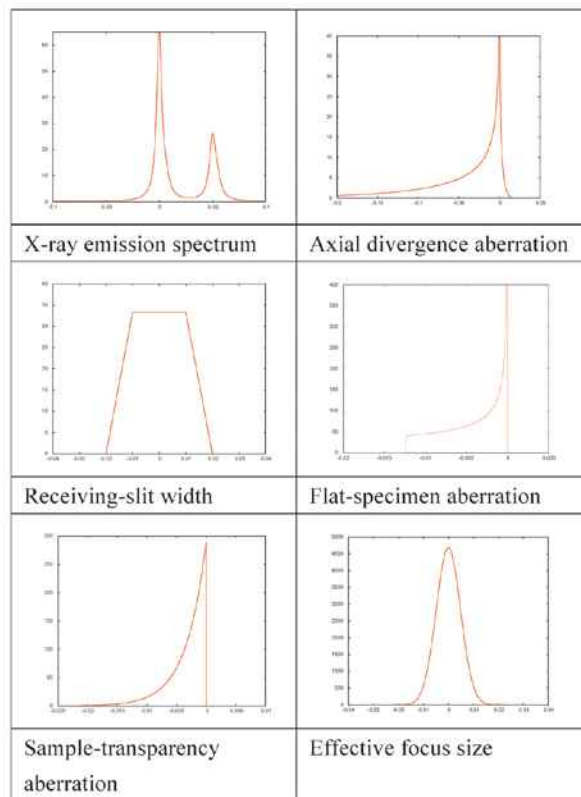


Fig. 3. Typical profile shapes for each instrumental aberration function.

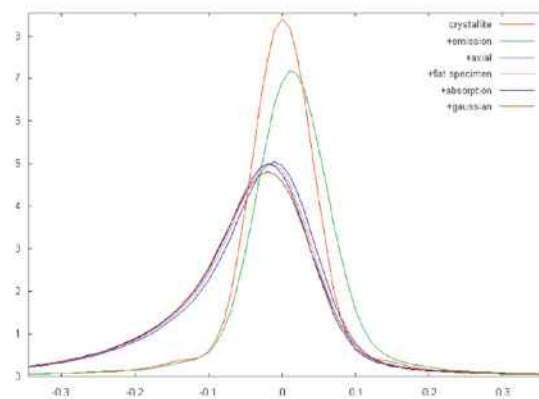


Fig. 4. Convolution of instrumental aberration functions.

Precise values of crystallite size, size distribution and strain are obtained by the least-square fitting to the measurement using the final profile convoluted all instrumental functions.

Although this convolution method itself is equivalent to that in the Rigaku software package, CSDA⁽⁴⁾, which can analyze crystallite size distribution, we apply a much faster convolution algorithm developed by R. W. Cheary *et al.* in PDXL that has achieved analysis times about fifty times faster than CSDA. Thus, we can apply this method to whole pattern fitting analysis and can obtain much reliable results compared with those by CSDA which analyzes only a single peak. In addition, lattice strain e , which cannot be refined using CSDA, can also be obtained simultaneously. In the next

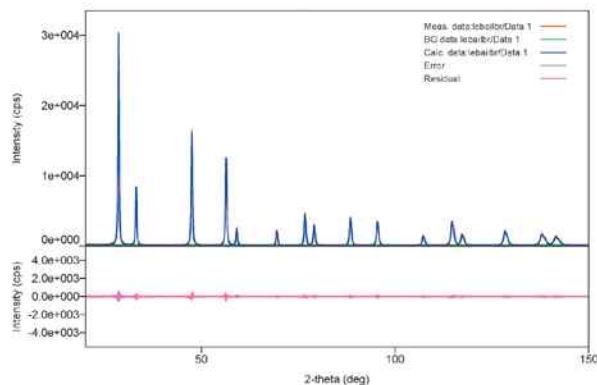


Fig. 5. Profile refined with the Pawley decomposition.

section, application examples using actual observations are shown.

4. Application

4.1. Size-strain round robin

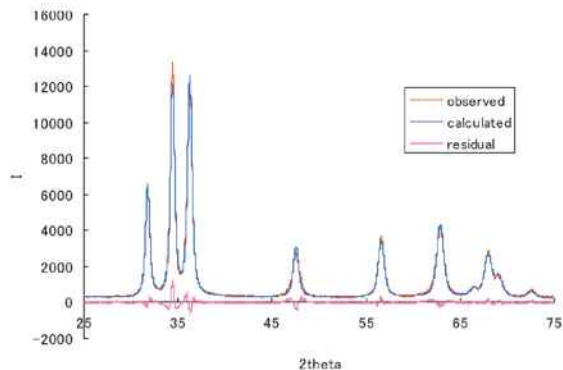
The commission on Powder Diffraction of the International Union of Crystallography held a size-strain round robin and published the results⁽⁵⁾. We analyzed one of the supplied data sets taken using Bragg-Brentano geometry in the University of Maine, among the observed data using PDXL. The Pawley decomposition, which treats the integrated intensities of diffraction lines as refinable parameters, is applied to the data. The refined profile is shown in Fig. 5. Red, blue and pink lines show measured profile, theoretical profile and their residuals, respectively. Figures of the refinement are $R_{wp}=5.96\%$ and $S=1.412$. The results give a volume averaged mean diameter of 30.16(4) nm, normalized size distribution deviation of 0.411(2) and lattice strain of 0.027(2)%. In the report of the round robin, diameter and its distribution deviation are summarized in Tables 2 and 3. Results in Table 2 are obtained with profile fitting to the deconvoluted profile by Richardson algorithm. D_V in the paper is called “apparent domain size” and defined the next formula⁽⁶⁾.

$$D_V = \frac{1}{V} \iiint t \, dx \, dy \, dz$$

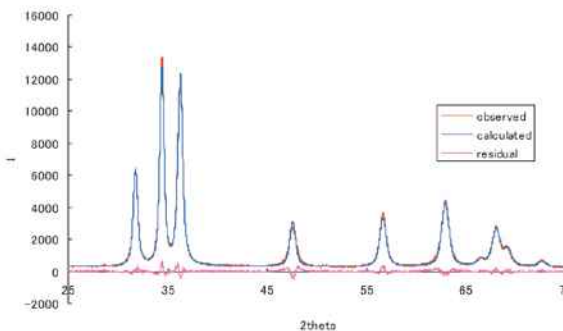
Here, V is the volume of a crystallite and t is the thickness of a crystallite parallel to the diffraction vector through (x, y, z) . Applying this to a spherical crystallite with diameter D , we obtain,

$$D_V = 3D/4.$$

With this formula, volume weighted mean diameter $D=30.16(4)$ nm is converted to $D_V=22.62(3)$ nm, which is almost the same as the reported value. Square of the size distribution deviation C corresponds to the dispersion c and the value 0.169(2) is only slightly smaller than the reported value. In addition, the results of the Warren-Averbach analysis are summarized in Table 3 of the report. The results show that the correlation between strain and size distribution is



(a)



(b)

Fig. 6. Pawley fitting assuming (a) spherical crystallite and (b) ellipsoidal crystallite for ZnO nanocrystalline.

relatively strong and that it is difficult to separate them. In PDXL, it is realized by refining both parameters simultaneously using the whole profile pattern.

4.2. Application to sample with anisotropic crystallite

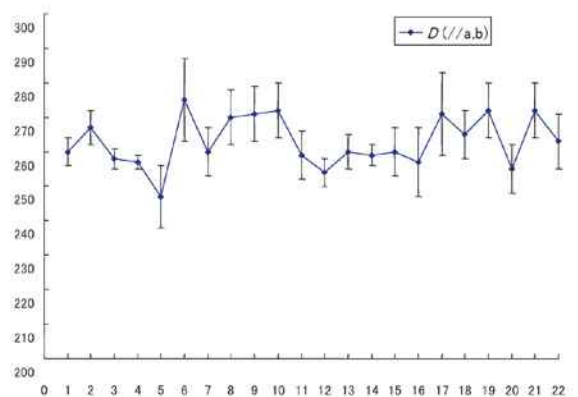
Next, we show an analysis of an anisotropic crystallite. When a crystallite has anisotropy, its diameter depends on the Miller indices. Assuming ellipsoidal shape for a crystallite, the (h, k, l) dependence of the diameter is given as⁽⁸⁾,

$$\frac{1}{D_h^2} = \frac{h^2 D_{3g}^2}{h^2} = \frac{b_{11}h^2 + b_{22}k^2 + b_{33}l^2 + 2b_{12}hk + 2b_{13}hl + 2b_{23}kl}{h^2 a^{*2} + k^2 b^{*2} + l^2 c^{*2} + 2hka^*b^* \cos \gamma^* + 2hla^*c^* \cos \beta^* + 2klb^*c^* \cos \alpha^*}$$

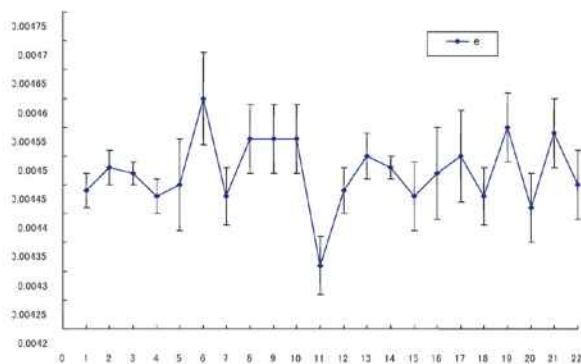
Here we analyze a measurement of the ZnO nanocrystalline material using Bragg-Brentano geometry. In Fig. 6(a), the refined profile assuming spherical crystallites is plotted ($R_{wp}=6.53\%$, $S=1.65$ and $D=30.9$ nm). The residual plot around the second and third peaks indicates the existence of anisotropy in the crystallite, because the second theoretical peak is sharper and the third theoretical peak is broader than those of the observed peaks. In Fig. 6(b), the refined profile assuming ellipsoidal crystallites is shown ($R_{wp}=6.31\%$, $S=1.595$, $D=25.9$ nm in a, b -axis direction and $D=33.8$ nm in c -axis direction). Since the residual is decreased when an anisotropic crystallite is assumed, an

Table 1. Measurement conditions. Soller slit angle is 5 degrees for No. 1–11 and 2.5 degrees for No. 12–22.

No.	1,12	2,13	3,14	4,15	5,16	6,17	7,18	8,19	9,20	10,21	11,22
Scan mode	cont.	step	cont.	cont.	cont.	step	cont.	cont.	cont.	cont.	cont.
Step[deg]	0.02	0.02	0.01	0.05	0.1	0.1	0.05	0.05	0.05	0.05	0.05
DS,SS[deg]	2/3	2/3	2/3	2/3	2/3	2/3	2/3	2/3	2/3	1/3	1
RS[mm]	0.1	0.1	0.1	0.1	0.1	0.1	0.05	0.2	0.3	0.1	0.1



(a)



(b)

Fig. 7. Results of (a) crystallite size and (b) strain for ZnO nanocrystalline under 22 instrumental conditions (Table 1). Horizontal axis expresses the condition number.

ellipsoidal crystallite model is more appropriate than a spherical model.

Next, we check the dependence of the results for the experimental conditions. One of the merits of the FP method is that the results are not influenced by experimental conditions without correction from the standard sample observation. Reproducibility of the

results should be checked. In the Table 1, the 22 types of measurement conditions are summarized. Here, we change the angular apertures of the Soller slit, scan mode (continuous scan or step scan), apertures of divergence slit (DS) and scattering slit (SS), and receiving slit (RS) width. Soller slit angle is 5 degree for No. 1–11 and 2.5 degree for No. 12–22.

Results are shown in Fig. 7. (a) is a plot of the volume averaged mean diameter perpendicular to *c*-axis direction. (b) is that of lattice strain. Horizontal axis is the condition number. Their error bars show the estimated standard deviations (1 sigma) of the least square refinement. It is shown that the values are comparable to their standard deviation with a high degree of reproducibility.

5. Summary

In this report, crystallite size, size distribution and strain studies using the FP method implemented in PDXL 2 and its underlying theory are described. The results obtained by analyzing the data of the size-strain round robin are almost consistent with of the data in the round robin report. We also apply the FP method to analysis of ZnO nanocrystalline and find that the ellipsoidal crystallite model is more suitable to explain the experiment and check the reproducibility of the results under multiple experimental conditions. This report finds that the reproduced analysis results were in agreement with estimated standard deviations.

In PDXL 2, more reliable analysis results can be obtained much easier than the ordinary method, which require the use of standard samples. We hope that PDXL will be utilized for material developments and contribute to the progress of material science.

References

- (1) R. W. Cheary and A. Coelho: *J. Appl. Cryst.*, **25** (1992) 109–121.
- (2) *The Rigaku Journal (English version)*, **28** (2012), No. 1, 29–30.
- (3) J. I. Langford and A. J. C. Wilson: *J. Appl. Cryst.*, **11** (1978), 102–113.
- (4) *The Rigaku Journal (English version)*, **25**, (2008), No. 1, 23–24.
- (5) D. Balzar, N. Audebrand, M. R. Daymond, A. Fitch, A. Hewat, J. I. Langford, A. Le Bail, D. Louër, O. Masson, C. N. McCowan, N. C. Popa, P. W. Stephens and B. H. Toby: *J. Appl. Cryst.*, **37** (2004), 911–924.
- (6) R. Delhez *et al.*: *The Rietveld Method*, Ed. by R. A. Young, Oxford University Press, (1995), 136.
- (7) B. E. Warren and B. L. Averbach: *J. Appl. Phys.*, **21** (1950), 595–599.
- (8) B. E. Warren and B. L. Averbach: *J. Appl. Phys.*, **23** (1952), 497.
- (9) P. Scardi and M. Leoni: *J. Appl. Cryst.*, **32** (1999) 671–682.